



ISSN: 2321-2152

IJMECE

*International Journal of modern
electronics and communication engineering*

E-Mail

editor.ijmece@gmail.com

editor@ijmece.com

www.ijmece.com

The numerical modelling and simulation of a horizontal-axis water turbine for use on underwater mooring platforms

Mr. K. Kaleeswaran, Dr. B. Rajeshkumar, Dr. D. Saravanan, Mr. M. Balaji, Dr. Indra

Vijay Singh

Professor³ Assistant Professor^{1,2,4} Associate Professor⁵

kaleeswaran.k@actechnology.in, rajeshkumar.b@actechnology.in,

saravanan.d@actechnology.in, balaji.m@actechnology.in, indiravijay@actechnology.in

Department of MCT, Arjun College of Technology, Thamaraikulam, Coimbatore-Pollachi
Highway, Coimbatore, Tamilnadu-642 120

Abstract

Underwater Moored Platforms (UMPs) are set to receive power from a horizontal axis water turbine, allowing them to remain operational for an extended period of time. Opening the turbine's controlled blades to generate power is one way to charge the UMPs while they're moored. The turbine's power production, thrust, and wake characteristics are examined by three-dimensional Computational Fluid Dynamics (CFD) models. Specifically, the installation site's influence on the turbine's location is considered. The simulations, which are grounded in the Reynolds Averaged Navier-Stokes (RANS) equations, use the shear stress transport k-u turbulent model. The numerical method is confirmed by using data from earlier experiments. This turbine's power coefficient achieves its maximum of 0.327 when positioned near the UMP's tail, according to the modelling findings. Additionally, we discuss the wake and flow arrangement around the blade.

Introduction

UMPs, or underwater mooring platforms, are submerged structures that are tethered to the ocean floor by means of mooring cables. This sort of equipment is capable of several tasks and has a service life of months to years. Some examples of UMPs include moored mines and self-mooring autonomous underwater vehicles (AUVs) as well as subsurface buoys (oceanographic sensors, acoustic communication nodes, etc.) (Robert, 2010). Most UMPs nowadays are powered by batteries, which severely limits their installed operational time due to their limited energy capacity and the continuous drain

of power by the onboard electronics. The batteries in the M-3 moored mine, for instance, only have a 12-month lifespan (Andrew et al., 2009). Due to the high expenses involved with collecting, repowering, and redeploying distant devices, extending the operational life of UMPs may dramatically lower the cost for missions when a prolonged presence is required. Using energy harvested from renewable sources to replenish the batteries of these platforms may drastically reduce the frequency with which UMPs must be redeployed owing to power shortages. To the best of our knowledge, ocean devices have been powered by four types of ocean energy: solar energy harvested from the ocean's surface, ocean thermal energy, ocean wave energy, and ocean

Current energy. There is a family of underwater vehicles called Solar-powered AUVs (SAUVs) (Crimmins et al., 2006; Jalbert et al., 2003). An array of batteries, a charge controller, a microcontroller, and a gas gauge make up the rest of the power system. Long-term tasks like monitoring, surveillance, and station maintaining are ideal for these systems. This procedure cannot be used to recharge the UMPs since these vehicles must come to the surface to be charged. Ocean thermal energy has also been used to drive underwater gliders by researchers (Webb et al., 2001). Due to the low energy density of ocean thermal energy, vehicles traveling across a thermo cline must adopt saw tooth-shaped trajectories. Therefore, UMPs that are supposed to carry out fix-point monitoring underwater should not make use of ocean thermal energy. It has been shown that ocean sensor buoys can be powered by ocean wave energy (Jeannette, 2015). The Direct Drive System uses tiny electric generators directly powered by the heave motion of a surface buoy caused by waves. Both the horizontal

and vertical velocities in the water underneath a deep-sea wave drop exponentially with depth (Benoit, 2014). The conversion device should be placed close to the water's surface for maximum power output. Similar to solar power, wave power is not an ideal source of electricity for most UMPs. Places with reliable ocean currents are ideal for installing UMPs. The ocean current's kinetic energy offers a viable option for recharging the UMPs. To harness the power of the ocean current and recharge a moored AUV, Wenlong et al. (2013) developed a small vertical axis water turbine (VAWT) with adjustable blades. When extended, this turbine resembles the design of the Darrieus turbine. However, the AUV's hull disruption resulted in poor turbine efficiency, with a maximum coefficient of the averaged power of 0.1 being measured (Wenlong et al., 2013). The orientation of the turbine axis in relation to the direction of the water flow allows for a simple categorization of water turbines, which have been extensively employed for hydrokinetic power production. The VAWT, or cross-flow water turbine, spins on an axis that is perpendicular to the flow of water. In contrast, the HAWT's axis of rotation is perpendicular to the flow of water. In order to produce rotational torque, these turbines generally use a propeller-like design with two or three blades. It has been shown that VAWTs used on UMPs are not as effective as their horizontally-mounted equivalents (Wenlong et al., 2013).

Description of the HAWT

In this analysis, a self-mooring AUV UMP was taken into account. The autonomous underwater vehicle (AUV) is programmed to go to a certain mooring position, moor to the bottom, gather oceanographic data for a predetermined amount of time, and then detach from the mooring line and return to a predetermined egress point (Robert, 2010). With a maximum diameter of $DA = 0.5$ m and a length of $L = 7$ m (not counting the propeller), the UMP utilized in this research is a prototype developed at Northwestern Polytechnic University. The UMP's HAWT is built around three rotors, three lead screw mechanisms, and a Permanent Magnet (PM) generator with a PM rotor and PM stator. As can be seen in Fig. 1(a), the blade is controlled by a lead screw system that is powered by a servo motor. Using the motion concept of the slider crank mechanism, the blade may be opened or closed by adjusting the rotation direction of the servo motor. The PM stator remains stationary along the UMP's central axis, while the PM rotor, blades, servo

motors, and lead screw mechanisms are assembled into a unit that spins around the PM stator's axis. When the blades are fully open, the turbine functions like a HAWT, with the lift from the blades driving the PM rotor. When the blades are closed, they nestle snugly into the UMP's hull grooves without interfering with the device's other operations. In Fig. 1(b), the HAWT is shown attached to the UMP. After a successful mooring, the HAWT's internal servo motors will activate, opening the rotors. At the same time, the UMP's center of gravity is lowered and the roll torque from the turbine is resisted by a hefty bar that extends from the hull. The HAWT helps keep the car running while it's tethered, and that lets the UMP keep it there for longer. When the mooring phase is complete, the vehicle releases the mooring rope and returns to the exit point, where the servo motors spin in reverse to shut the blades. In this study, we explore a turbine that was developed with help from BEM theory. The turbine has a rotor diameter of $R = 0.75$ m and a rotor diameter of the hub of 0.25 m (the UMP hull's radii). With an input velocity of $U = 0.5$ m/s and a tip speed ratio of $TSR = 5$, the turbine was fine-tuned for maximum efficiency. Tip speed ratio is the relationship between the velocities of the tips of the rotor blades and the incoming air.

$$TSR = \frac{\omega R}{U}, \quad (1)$$

Table 1 Specification of the blade.

r/R	c/R	θ (deg)	t/c (%)
0.4	0.1600	10.0000	25
0.5	0.1600	10.0000	18
0.6	0.1433	7.5431	18
0.7	0.1266	5.6442	18
0.8	0.1133	4.1796	18
0.9	0.1025	3.0168	18
1	0.0935	2.0717	18

Turbine profiles based on NACA 63-4XX airfoils were selected. The NACA 63-4XX airfoils are cavitations-resistant and have a significant minimum pressure coefficient. The blade's effective length (from the rotor's hub to its tip) is 40%. At 40% spread, the blade is 25% thick relative to the cord, and it declines linearly to 18% at 50% span. The thickness of the blades is fixed at 18% beyond the

50% span. The blade's local radial location r , chord length c , twist angle q , and thickness t are summarized in Table 1. Note that $0.16R$ and 10 were the upper limits for chord length and twist angle, respectively. The chord length and twist angle of the blade must be small enough so that it may be installed in the UMP's hull. The hydrodynamic center of the blade is located at a chord length of 25% from the leading edge, which was used to calculate the placement of the blade's pivot point. The turbine's installation location (shown in Fig. 2) had to be established, despite the fact that its geometric specifications were already known. In contrast to conventional HAWTs, the turbine shown here has a significantly more compact hub in relation to the overall size of the UMP. As a result, the UMP housing will always have some effect on the turbine's efficiency. Locations behind the front of the UMP were used to determine the five installation sites examined and compared in the CFD simulations: $1/14$ $0.2L$, $1/14$ $0.4L$, $1/14$ $0.6L$, $1/14$ $0.7L$ and $1/14$ $0.8L$. In addition, two further examples ($1/14$ $0.4L$ and $1/14$ $0.7L$) are examined without rudders to explore the influence of the rudders. The UMP propeller is ignored in the simulations in order to simplify the simulation and minimize the amount of grid components. Cases used in the simulations are listed in Table 2.

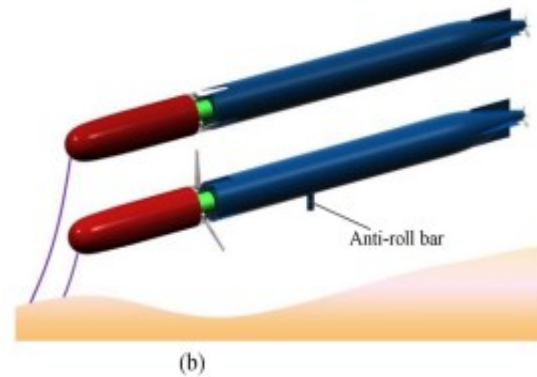
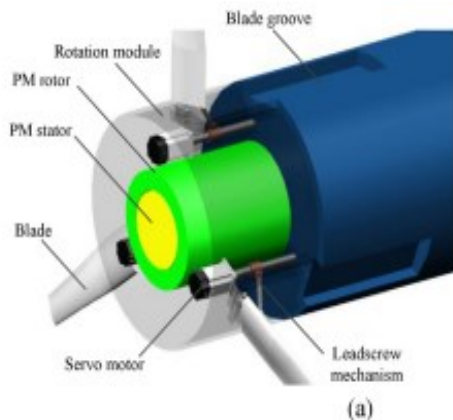


Fig. 1 (a) shows the HAWT's internal construction, and (b) depicts the turbine as it might appear on a UMP.

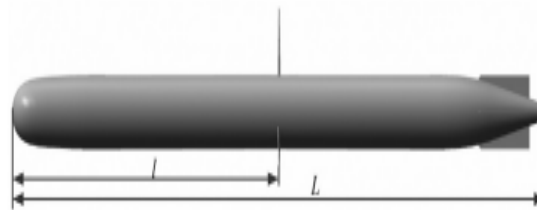


Fig. 2. Illustration of the installation position of the turbine.

Table 2 Simulation cases

Case	l/L	Other
1	0.2	With rudders
2	0.4	With rudders
3	0.6	With rudders
4	0.7	With rudders
5	0.8	With rudders
6	0.4	Without rudders
7	0.7	Without rudders

Numerical method

Using a second-order accurate finite-volume discretization approach, the incompressible RANS equations were solved using the commercial CFD package FLUENT v13.0. For this reason, the shear stress transfer (SST) $k-u$ turbulence model was used to represent the RANS equations' turbulence components. The SST $k-u$ turbulence model has been used successfully in the CFD simulation of wind/water turbines (Michael et al., 2011; Nak et al., 2015) due to its ability to accurately predict the onset

and amount of flow separation under adverse pressure gradients. To save time and resources, we employed a revolving reference frame model to approximate the rotor's rotation. This technique forms the governing equations for the rotor domain in a reference frame that rotates with the turbine, while the outer domain stays in a fixed coordinate system, simulating the rotor's rotation without physically rotating the grid (Michael et al., 2011).

3.1 Boundary conditions and computation domains

The computational domain in this simulation was scaled to permit complete upstream flow development while minimizing obstruction effects. We choose a cylinder with a radius of $8R$ and a length of $5.5L$ ($25.67D$) as our computational domain. The UMP was installed at the cylinder's middle, $3L$ ($14D$) from the downstream wall. The size of the domain and the grid's structure are shown in Fig. 3. Several prior studies (Michael et al., 2011; Monier et al., 2013; Tongchitpakdee et al., 2005; Nak et al., 2015) only simulated one blade of the turbine taking into account the periodicity of the rotor. However, because the UMP being studied here has three blades and four rudders, it would be insufficient to model only one of them. The whole realm was divided into thirds. The rotor domain is the first and it includes the grid components that are next to the rotor. The second domain is made up of the cells that are close to the UMP's tail. The last domain is the outer region's cells, found in the outer domain. The tail was detached from the UMP primarily to facilitate grid generation. At the domain's intake, a constant and uniform velocity profile of 0.5 meters per second was applied. It is well-established that turbulence intensity significantly affects a HAWT's behavior. While this parameter has a very little effect on average performance measures like torque and thrust, it has a significant impact on performance variability. As the turbulence strength grows, the wake fades away significantly more quickly (Mycek et al., 2014a). This article ignores the impact of turbulence intensity, choosing instead to simulate an intake with a constant turbulence intensity of 1% so as to concentrate on the effects of turbine locations.

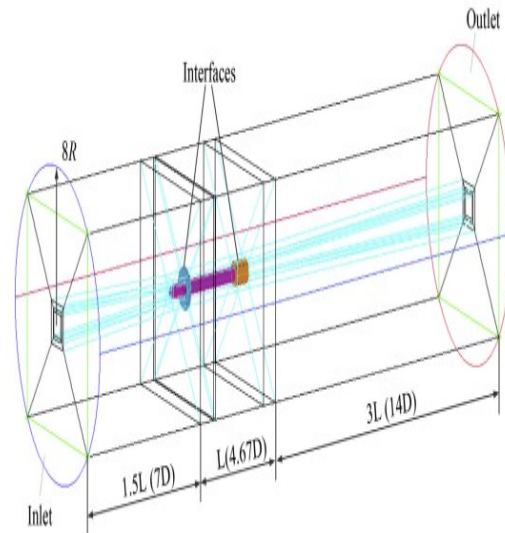


Fig. 3. Computation domains.

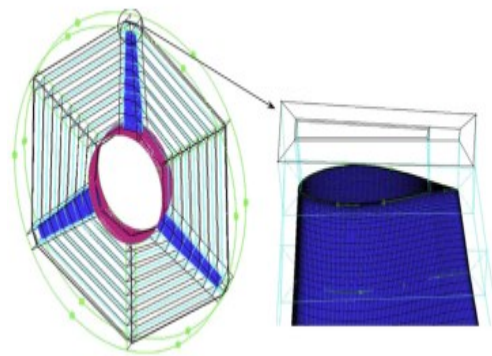


Fig. 4. Grid of the rotor sub domain.

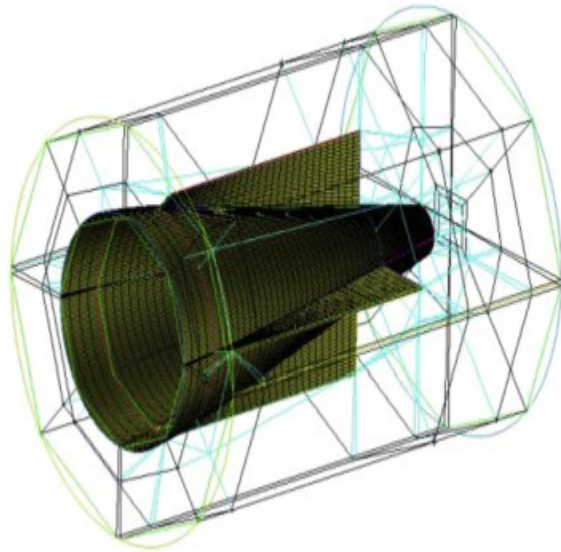


Figure 5: A tail sub domain grid.

To Create a Grid 3.2 It has been shown that using a structured hexahedral grid is preferable since it naturally produces highly accurate numerical solutions in CFD simulations (Michael et al., 2011). All structured grids used in this investigation were created with the help of the ICEM grid creation function included in ANSYS 13.0. All three sub domain grids were

Table 3 Torque determined at 0.2 L and 5 TSR.

Number	Radius of the domain	Approx. number of grid elements	Torque/Nm
1	8R	6.3E+06	10.76
2	8R	8.2E+06	10.69
3	8R	1.1E+07	10.66
4	16R	10.3 E+06	10.67

Made up of individual components that were later combined. The rotor domain has a greater density of grid nodes than the other domains. Higher grid resolution was applied to the region behind the rotor and close to the UMP's hull, where large velocity differences were anticipated. In order to enhance the grid quality and accurately depict the boundary layer flow, grid components in the shape of prisms were extruded from the blade's surfaces. Depending on the rotor's rotation speed and the element's location on the blade, the height of the first prism layer above the surface was adjusted such that the y value for the first elements from the wall was below 1. With such a low value of y, the SST k u turbulence model might be used effectively. All of the sub domains' mesh growth

rates were set to 1.2. The rotor sub domain topology and the tail sub domain topology are shown in Figs. 4 and 5, respectively. For the purpose of the grid resolution analysis, three grids were created. The grid resolution on the blades and behind the rotor is where you'll see the most difference between the two.

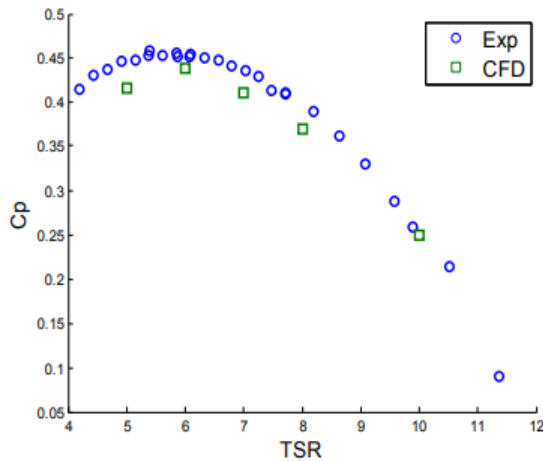
4. Numerical method verification and validation

4.1. Verification

The effect of grid resolution and domain size on rotor torque was investigated by means of separate studies. Case 1 turbine from Table 2 was simulated with a TSR of 5. Torques computed at various grid resolutions and domain sizes are summarized in Table 3. The first three findings show that the outcomes were quite similar for grids of 8.2E06 and 1.1E07 elements. This suggests that CFD-predicted rotor torque is somewhat insensitive to changes in grid resolution. Grid resolution is the same as in No. 2, but the No. 4 domain is 16R bigger. The resulting torques from these two scenarios is not drastically different from one another. When the domain's radius is greater than 8R, we may safely disregard the obstructive impact of its borders. Time efficiency in simulation led to the selection of an 8.2E06 element grid and an 8R element domain for the subsequent runs.

Table 4: Verification under simulated conditions.

Parameters	Value
Number of blades	3
Blade section	NACA63-8XX
Diameter of the turbine	0.8 m
Inflow velocity	1.73 m/s
TSR	5–10



Validation of the numerical approach shown in Fig. 6.

Verification 4.2 CFD simulations of the HAWT were carried out in Bahaj et al. (2007a, b) to verify the reliability of the approach employed in this study. The experimental data from Bahaj et al.'s cavitation tunnel is compared with the numerical findings. Table 4 details the experimental model's conditions. Figure 6 displays the comparison between CFD and experimental data for the coefficient of power at various TSRs. Here is how we characterize the power coefficient:

$$C_p = \frac{P}{0.5\rho\pi R^2 U^3}, \quad (2)$$

5. Results and discussion

5.1. Torque and power characteristics

The power coefficient curves for various turbine installation sites are shown in Fig. 7(a). In all but one of the five rudder modeling scenarios, the curves follow the same pattern over the range of measured tip speed ratios. At TSR 14 2, when the rotor blades are in deep stall, all examples have a minimum Cp value of about 0.03. The Cp curves rise with TSR, peaking at TSR 14 5, and then falling off precipitously after TSR 14 6. The Cp curve for the case of $l = 0.4L$ is the lowest of the five and peaks at TSR = 6. The Cp curve decreases gradually when TSR is increased, and its size is almost double that of the other four examples. For TSRs 4 and 5, higher

turbulence intensity upstream from the rotor causes a loss of power of 14 0.4L. The UMP's divided flow at its snout expands axially, and turbulence gets more severe. Cross-sectional planes, located 0.1R upstream of the rotors, are shown in Fig. 8 together with the contours of turbulence intensity. Figure 8 shows how the turbulence increases in intensity around the rotors' roots. It is well established that the coefficient of power decreases with increasing turbulence intensity (Mycek et al., 2014a, b). Cp values for TSRs 4 and 5 did not decrease for 14 0.6L, 14 0.7L, and 14 0.8L, despite considerably greater turbulence intensity than for 14 0.4L. The proximity of the turbines in these circumstances to the rudders explains why they are so resistant to turbulent upstream velocity conditions: rudders act as rectifying plates, limiting the rotational flow in the wake. Additional instances 14 0.4L (case 6) and 14 0.7L (case 7) were utilized to

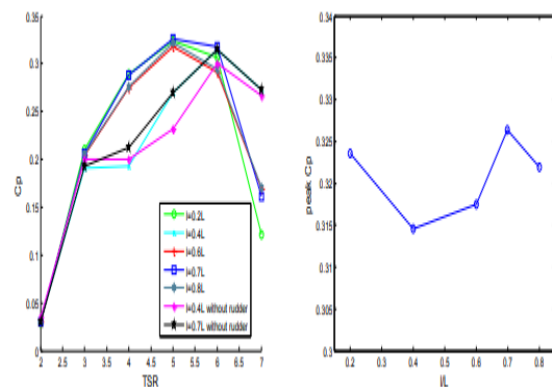


Fig. 7. The results of Cp: (a) Cp vs. TSR and (b) peak Cp vs. l.

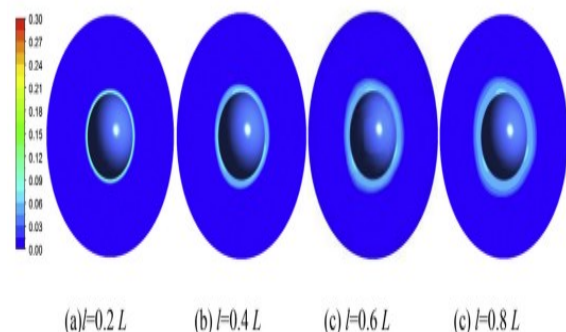
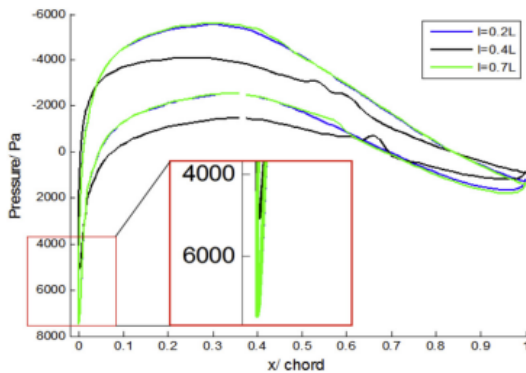
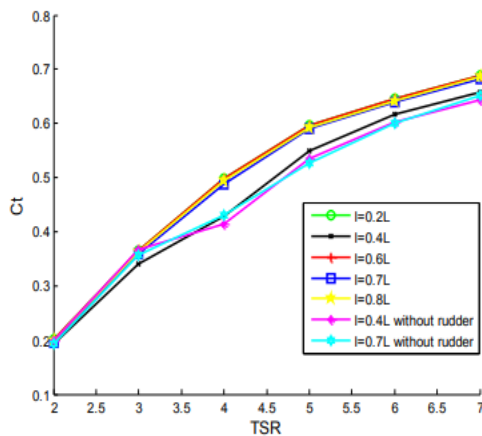


Figure 8: Cross-sectional intensity contours of turbulence at TSR = 5 for $l = 0.2L$, $0.4L$, $0.6L$, and $0.8L$ upstream of the turbines.



As seen in Figure 9, this is corroborated by the pressure pattern on 90% span sections at TSR 14.7. By comparing the C_p curves at $l = 0.4L$ and $l = 0.4L$ without rudder in Fig. 7, we conclude that the turbine hardly noticed the rudder influence at $l = 0.4L$. In Fig. 7, we see that the C_p is definitely enhanced owing to the rudder effect by comparing the C_p curves at $l = 0.7L$ with $l = 0.7L$ without rudder. This result constitutes a



Using Fig. 10's thrust-to-tip-speed ratio as a reference, we may decide whether to locate the turbine close to the nose, where the turbulence intensity is low, or close to the tail, where the rudder effect is high. Figure 9 shows the pressure distribution, which explains why the C_p is so high ($l = 0.4L$) at TSR 14.7. The pressure pattern at 90% span sections at TSR 14.7 is shown in Fig. 9. The pressure and suction sides of the blade are subjected to more force in the $l = 0.4L$ case than in the $l = 0.2L$ and $l = 0.7L$ examples, but the net pressure difference is negligible. The maximum pressure at the leading edge (x/c near zero) is about 2500 Pa higher for instances of $l = 0.2L$ and $l = 0.7L$ compared to cases of $l = 0.4L$. Because of the

increased pressure at the leading edge, there will be more drag and, therefore, less torque and power. Peak C_p values vary as a function of l , as seen in Fig. 7(b). In the limit of $l = 0.7L$ and $TSR = 5$, the maximum C_p of 0.327 is attained. Wenlong et al. (2013) calculated a VAWT for UMPs, and their results showed a value of just 0.10. Both $l = 0.2L$ and $l = 0.8L$ have lower C_p values than $l = 0.7L$. Peak C_p is lowest (0.315) at $l = 0.4L$.

5.2. Flow near the blade

Case 1, 2, and 4 are shown in Fig. 11 together with their respective pressure distributions and limiting streamlines on the pressure and suction sides of the blade. We choose the nose, the midsection, and the tail to show the range of possibilities. Fully connected flow is seen on much of the pressure surface of the blade at low tip speed ratio (TSR 14.2).

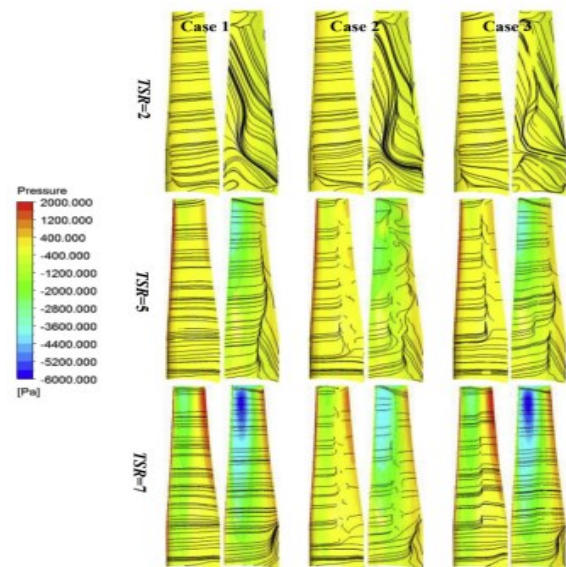


Figure 11 shows the pressure distribution along the blade and the limiting streamlines on each side of the blade for a variety of tip speed ratios. The whole suction side of the blade experiences a high rate of separation flow. Figure 12 displays pressure streamlines and contours for the chosen sections at TSR 14.2. All regions exhibiting unstable shedded vortices provide excellent examples of the separation flow. When the blade's span is between 50 and 90 percent, the flow breaks away from the leading edge and reattaches to the suction side. The flow splits into two counter-rotating vortices at 70% span, having previously been attached to the leading and trailing edges. When comparing examples at TSR 14.5 and TSR 14.7, we find that the shedding of the vortices

results in a large pressure recovery on the suction surface.

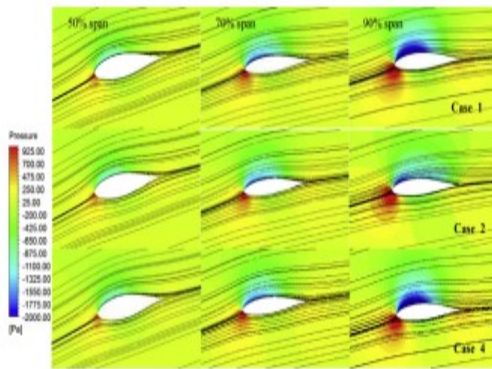
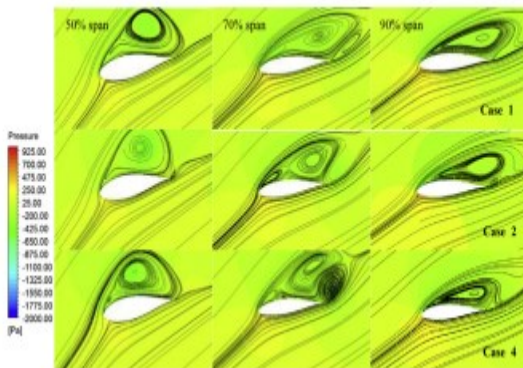


Fig. 13. Streamlines and contours of pressure on the selected sections at TSR $\frac{1}{4}$ 5.



Pressure contours and streamlines along the chosen portions at TSR 14 2 are shown in Fig. 12.

Only example 1 (l 14 0.2 L) forecasts completely connected flow at TSR 14 5 and on the pressure surface. In the other three scenarios, radial flow is seen at positions greater than 50% span and about 50% chord. Suction side flow separation is always minimal, beginning at the wingtip and continuing to within a few percent of the wingtip's trailing edge (about 80% of the chord). However, in example 2 (l 14 0.4L), the flow is more turbulent before the separation point, resulting in a pressure recovery on the suction surface. Figure 13 displays this information graphically, with pressure contours and streamlines for the chosen portions. The limiting streamlines follow the same pattern as at TSR 14 5 but to a lesser extent at TSR 14 7 and on the pressure surface. On the suction side, however, the predictions for both case 1 (l 14 0.2L) and case 4 (l 14 0.7L) are for entirely connected flow everywhere save a little

region close to the root. In example 2 (l 0.4L), radial flow is also detected at about the 50% chord location in addition to the connected flow. Pressure contours and streamlines along the chosen sections at TSR 14 7 are shown in Fig. 14. Positive pressure at the leading edge and trailing edge increases compared to Figs. 11 and 12, whereas negative pressure on the sides of the blade shifts in the opposite direction due to the higher inflow velocity and lower angle of attack.

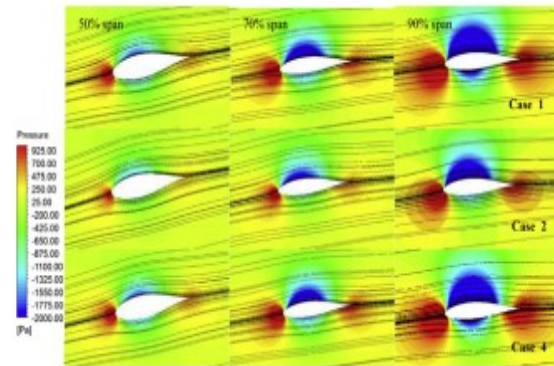


Fig. 14. Streamlines and contours of pressure on the selected sections at TSR $\frac{1}{4}$ 7.

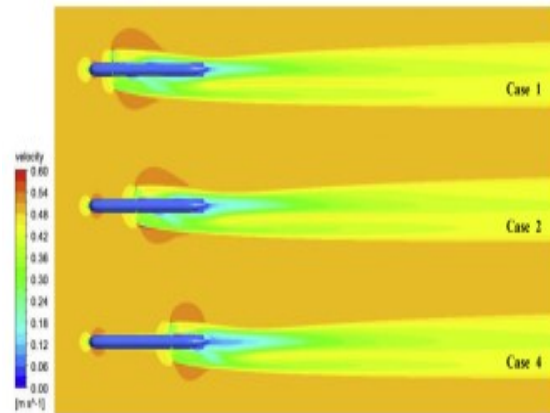


Fig. 15. Contours of velocity at the lateral cross-section planes at TSR $\frac{1}{4}$ 5.

5.3. Wake properties

For cases 1, 2, and 4, at TSR 14 5, the axial velocity contours at the lateral cross-section planes are shown in Fig. 15. A low-velocity zone is created behind the turbine when the upstream fluid is slowed as it passes through. For all scenarios, regardless of turbine

installation location, this low-velocity zone extends to up to around 6D downstream of the turbine. Downstream of the blade's leading edge, a narrow region of high speed is seen. In cases 1 and 2, this high-velocity zone is almost the same size, while in example 4 it is much bigger. The furthest reaches of the four situations show no discernible variation. A small axial strip experiences a disturbance in velocity; this strip gradually grows in size along the flow direction, reaching a maximum size of roughly 1.8D at 3L downstream of the UMP. Approximately 90% of the initial inflow velocity is restored by the time the axial velocity reaches the 3L after the UMP.

6. Conclusion

This research showed a water turbine with a horizontal axis that might be used in UMPs. This sort of turbine was modeled in three dimensions using CFD software. The impact of installation location on turbine performance was investigated after the verification and validation of the numerical approach. The following findings were uncovered: 1) For a rotor with a design TSR of 5, as in the 14 0.7L example, the maximum C_p is 0.327, which is more than three times bigger than that of a VAWT originally designed for UMPs. The rudders may make the turbine resistant to the effects of high upstream velocities in turbulent water. Wakes in all circumstances are the same. At 3L downstream from the UMP, the axial velocity in the wake is disrupted in a restricted axial strip that grows in size along the flow direction to roughly 1.8D in width. This study approximated the turbine's rotation around a stationary axis and disregarded the UMP's motion. The performance of the turbine under yaw situations, as well as the interaction between the turbine and the UMP, will be the subject of future research.

References

Andrew, E., Lyle, G., William, M., 2009. *Chinese Mine Warfare-a PLA Navy 'Assassin's Mace' Capability*. US Naval War College, Rhode Island.

Bahaj, A., Molland, A., Chaplin, J., Batten, W., 2007a. *Power and thrust measurements of marine current turbines under various hydrodynamic flow conditions in a cavitation tunnel and a towing tank*. *Renew. Energy* 32, 407e426.

Bahaj, A., Batten, W., McCann, G., 2007b. *Experimental verifications of numerical predictions for the hydrodynamic performance of horizontal axis*

marine current turbines. *Renew. Energy* 32, 2479e2490.

Benoit, C., 2014. *Environmental Fluid Mechanics*. John Wiley & Sons, Inc. Burton, T., Sharpe, D., Jenkins, N., Bossanyi, E., 2001. *Wind Energy Handbook*. John Wiley & Sons Ltd.

Crimmins, M., Patty, T., Beliard, A., et al., 2006. *Long endurance test results of the solar-powered AUV system*. In: *OCEANS 2006*, pp. 1e5. Boston, MA.

Coiro, P., Maisto, U., Scherillo, F., et al., 2006. *Horizontal axis tidal current turbine: numerical and experimental investigations*. In: *Owemes 2006*. Civitavecchia, Italy.

Epps, P., Stanway, J., Kimball, W., 2009. *An open-source design tool for propellers and turbines*. In: *Society of Naval Architects and Marine Engineers Propeller/Shafting '09 Symposium*, Williamsburg, VA.

Galloway, P., Myers, L., Bahaj, A., 2011. *Experimental and numerical results of rotor power and thrust of a tidal turbine operating at yaw and in waves*. In: *World Renewable Energy Congress 2011*, pp. 2246e2253. Linkoping, Sweden.

Hand, M., Simms, D., Fingersh, L., et al., 2001. *Unsteady Aerodynamics Experiment Phase VI: Wind Tunnel Test Configurations and Available Data Campaigns*. NREL/TP-500e29955, Colorado.